




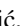













Properties of an organic model $S = 1$ Haldane chain system

Ivan Jakovac ¹, Tonči Cvitanić ¹, Denis Arčon ^{2,3}, Mira Herak ⁴, Dominik Cinčić ⁵, Nea Baus Topić ⁵, Yuko Hosokoshi ^{6,7}, Toshio Ono ^{6,7}, Ken Iwashita ⁷, Nobuyuki Hayashi ⁶, Naoki Amaya ⁶, Akira Matsuo ⁸, Koichi Kindo ⁸, Ivor Lončarić ⁹, Mladen Horvatić ¹⁰, Masashi Takigawa ⁸ and Mihael S. Grbić ^{1,*}

¹Department of Physics, Faculty of Science, University of Zagreb, Bijenička cesta 32, 10000 Zagreb, Croatia

²Jozef Stefan Institute, Jamova cesta 39, SI-1000 Ljubljana, Slovenia

³Faculty of Mathematics and Physics, University of Ljubljana, Jadranska 19, SI-1000 Ljubljana, Slovenia

⁴Institute of Physics, Bijenička cesta 46, 10000 Zagreb, Croatia

⁵Department of Chemistry, Faculty of Science, University of Zagreb, Horvatovac 102a, 10000 Zagreb, Croatia

⁶Department of Physics, Osaka Metropolitan University, Osaka 599-8531, Japan

⁷Department of Physical Science, Osaka Prefecture University, Osaka 599-8531, Japan

⁸Institute for Solid State Physics, The University of Tokyo, 5-1-5 Kashiwanoha, Kashiwa, Chiba 277-8581, Japan

⁹Ruđer Bošković Institute, Bijenička cesta 54, 10000 Zagreb, Croatia

¹⁰Laboratoire National des Champs Magnétiques Intenses, LNCMI-CNRS (UPR3228), EMFL, Université Grenoble Alpes, UPS and INSA Toulouse, Boîte Postale 166, 38042 Grenoble Cedex 9, France



(Received 25 October 2024; accepted 10 January 2025; published 3 February 2025)

We present the properties of an organic $S = 1$ antiferromagnetic chain system $m\text{-NO}_2\text{PhBNO}$ (abbreviated BoNO). In this biradical system, two unpaired electrons from aminoxyl groups are strongly ferromagnetically coupled ($|J_{\text{FM}}|/k_B \gtrsim 500$ K), which leads to the formation of an effective $S = 1$ state for each molecule. The chains of BoNO biradicals propagate along the crystallographic a axis. Temperature dependencies of the g factor and electron paramagnetic resonance (EPR) linewidth are consistent with a low-dimensional system with antiferromagnetic interactions. The EPR data further suggest that BoNO is a Haldane system with an almost isotropic g factor ($2.0023 \pm 2\%$). The magnetization measurements in magnetic fields up to 40 T and low-field susceptibility, together with ^1H nuclear magnetic resonance (NMR) spectra, reveal a dominant intrachain antiferromagnetic exchange coupling of $J_{1\text{D}}/k_B = (11.3 \pm 0.1)$ K, and attainable critical magnetic fields of $\mu_0 H_{c1} \approx 2$ T and $\mu_0 H_{c2} \approx 33$ T. These measurements therefore suggest that BoNO is a rare example of a Haldane system with extremely small magnetic anisotropy. The present results are crucial for a future in-depth NMR study of the low-temperature Tomonaga-Luttinger liquid and magnetic field-induced phases, which can be performed in the entire phase space.

DOI: [10.1103/PhysRevB.111.064407](https://doi.org/10.1103/PhysRevB.111.064407)

I. INTRODUCTION

In low-dimensional quantum spin systems, enhanced quantum fluctuations enable a multitude of ground states that cannot be realized in three-dimensional systems. The concurrent development of theoretical analyses and experimental realizations of these systems has enabled great leaps in the understanding of many-body quantum effects. Ground-state properties can be modeled by considering the spin value, geometry, and strength of interactions, and the interplay of various types of interactions. Testing of such models allows a thorough examination of quantum phenomena; indeed a multitude of knowledge has been gained by studying the ideal $S = 1/2$ chain material $\text{Cu}(\text{C}_4\text{H}_4\text{N}_2)(\text{NO}_3)_2$ (CuPzN) [1,2], the transverse field Ising chain system CoNb_2O_6 [3,4], the strong-rung and strong-leg two-leg spin-ladder systems $(\text{C}_5\text{H}_{12}\text{N}_2)\text{CuBr}_4$ (BPCB) [5–7] and $(\text{C}_7\text{H}_{10}\text{N})_2\text{CuBr}_4$ (DIMPY) [8–10], respectively, and the large- D system $\text{NiCl}_2\text{-4SC}(\text{NH}_2)_2$ (DTN) [11–13]. The last three systems were critical in the context of studying magnetic field-induced

long-range order of Bose-Einstein condensate (BEC) type [14–16].

Among the chain models, a unique ground state emerges for a simple Hamiltonian $H = J_{1\text{D}} \sum_{ij} \mathbf{S}_i \mathbf{S}_j$ with integer-valued spins \mathbf{S}_i , where nearest neighbors interact via Heisenberg antiferromagnetic interaction $J_{1\text{D}}$. Haldane has shown [17,18] that in this case, the ground state is singlet with an energy gap Δ to the first excited (triplet) state. This state, also called the Haldane phase, is topologically distinct from its half-integer spin counterpart in which a gapless Tomonaga-Luttinger liquid (TLL) forms. The Haldane phase has been shown to be stable in the presence of a finite interchain coupling and single-ion anisotropy [19,20], which are typically unavoidable in any realistic material. Over the years, there have been many candidate materials for the realization of the Haldane state, with $S = 1$ spin borne by transition-metal ions such as archetypical CsNiCl_3 , AgVP_2S_6 , $\text{Ni}(\text{C}_5\text{D}_{14}\text{N}_2)_2\text{N}_3(\text{PF}_6)$ (NDMAP), $\text{Ni}(\text{C}_2\text{H}_8\text{N}_2)\text{NO}_2(\text{ClO}_4)$ (NENP), and $\text{PbNi}_2\text{V}_2\text{O}_8$. However, although they all host the Haldane phase in zero magnetic field, they are not suitable [21,22] for expanding the research and studying the evolution of the Haldane phase into the magnetic field-induced BEC. To realize the BEC phase, an external magnetic field must first be applied to lower the energy

*Contact author: mgrbic.phy@pmf.hr

of the triplet state and close the (Haldane) gap at $\mu_0 H_{c1} = \Delta/g\mu_B$, which reestablishes the TLL state. If the spin system is U(1) symmetry invariant, the BEC ground state emerges with further increase of the magnetic field until the system becomes fully polarized at $g\mu_0\mu_B H_{c2} \approx 4k_B J_{1D}$. The latter symmetry condition is difficult to fulfill since the spin-orbit effects of transition-metal ions add symmetry-breaking terms into the Hamiltonian that cannot be neglected. The available number of candidates is further reduced to none when one looks for those where magnetic interaction J_{1D} allows for the entire phase diagram to be accessible in a laboratory.

Recently, molecule-based magnetic systems have attracted attention [23,24] as one can control the energy scale of exchange interactions. Among them, purely organic radical spin systems are of particular interest, as the delocalized nature of electron orbitals ensures the isotropy of the spin Hamiltonian and spin-orbit coupling is weak compared to transition-metal systems. The high-spin ($S \geq 1$) systems are formed due to favorable intramolecular spin couplings in certain stable nitroxide-based radicals [25–29]. Relatively simple π -conjugated biradicals with favorable intramolecular ferromagnetic coupling function as $S = 1$ building blocks for modeling spin-chain systems [30]. For example, *m*-phenylene-bis(*N*-*tert*-butylaminoxyl), abbreviated as BNO, has been shown to have a large ferromagnetic intramolecular interaction of $|J_{FM}|/k_B \geq 600$ K [31,32]. When arranged into different crystal lattices, these molecules form an effective one-dimensional (1D) or two-dimensional (2D) system [33,34]. Here, the passive substituents are used to define the crystal structure and the apparent dimensionality of the system. In contrast to numerous manifestations of the Haldane systems in organometallics, no $S = 1$ nitroxide system has so far displayed suitable quasi-1D geometry [29].

In this study, we present a molecular radical system 3,5-bis(*N*-*tert*-butylaminoxyl)-3'-nitro-1,1'-biphenyl (*m*-NO₂PhBNO, hereafter abbreviated as BoNO). Our experimental data demonstrate that BoNO is an excellent candidate for a Haldane system, due to BNO $S = 1$ units arranged in chains, with intermolecular antiferromagnetic coupling $J_{1D}/k_B \approx 11.3$ K, which is almost two orders of magnitude smaller than the intramolecular $|J_{FM}|$. The molecular and crystal structure is determined by the high-resolution single-crystal x-ray measurements. We have combined multiple experimental techniques: bulk magnetization, magnetic susceptibility, electron paramagnetic resonance (EPR) measurements, and density functional theory (DFT) calculations. When the data are compared to the existing theoretical density-matrix renormalization group (DMRG) and quantum Monte Carlo (QMC) calculations, we demonstrate that BoNO is a fitting candidate for an isotropic Haldane system. Additionally, ¹H nuclear magnetic resonance (NMR) spectral analysis reveals a strong hyperfine coupling between the $S = 1$ system and the probed ¹H nuclei, paving the way for an extensive ¹H NMR research of the low-temperature spin dynamics in the TLL and BEC phases.

II. METHODS

BoNO was synthesized by following the conventional procedure [26] starting from 1,3,5-tribromobenzene, via Suzuki

coupling with 3-nitrophenylboronic acid, followed by treatment with freshly prepared Ag₂O. The obtained material was purified by column chromatography on silica gel with diethyl ether and *n*-hexane. Recrystallization of slow evaporation from a concentrated mixed solution of diethyl ether and *n*-hexane at room temperature yielded red plate single crystals of BoNO. The typical crystal size was $4 \times 1 \times 0.2$ mm³.

The crystallographic data were collected on an Oxford Xcalibur 3 diffractometer using the Mo K α ($\lambda = 0.71$ Å) radiation source. The $2 \times 1.5 \times 0.2$ mm³ sample was epoxy-glued on a 4-circle κ -goniometer and measured at $T = 100$ and 300 K in a dry nitrogen current. The data collection and cell refinement were performed by CRYSTALIS software; the structure was solved by the direct methods and refined anisotropically using the SHELX software suite [35]. The missing hydrogen atom positions were refined using the universal force field molecular optimization.

DFT calculations were performed using a plane-wave code QUANTUM ESPRESSO [36] with the van der Waals density functional with consistent exchange (vdW-DF-cx) [37] and the so-called Garrity-Bennett-Rabe-Vanderbilt (GBRV) pseudopotentials [38], with an energy cutoff of 40 Ry for the plane-wave basis set. Atom positions were relaxed until forces on each atom were below 0.03 eV/Å, with the unit cell fixed to the experimental one.

The low-field dc magnetization measurements were performed using the Quantum Design MPMS3 magnetometer on a $m = 69 \pm 6$ μ g sample. Magnetic susceptibility was obtained by dividing the measured magnetization by the applied magnetic field and multiplying by Mmol/m (Mmol = molar mass, m = mass of the sample).

The high-field magnetization at pulsed magnetic fields of up to about 40 T was measured using a nondestructive pulse magnet at the Institute for Solid State Physics at the University of Tokyo. All experiments were performed using small randomly oriented single crystals with typical dimensions of $1 \times 1 \times 0.2$ mm³.

X-band (~ 9.6 GHz) EPR experiments were performed on cooling of BoNO single crystals mounted on a glass sample holder and sealed under a dynamic vacuum in standard Suprasil quartz tubes ($OD = 4$ mm) with a Bruker Elexsys E500 EPR spectrometer equipped with a TEM104 dual-cavity resonator, and an Oxford Instruments ESR900 cryostat with an ITC503 temperature controller (stability ± 0.05 K). The typical microwave power was set to 0.1 mW, while the modulation field was set to the amplitude of 0.02 mT and a modulation frequency of 100 kHz.

For the NMR study, we used a rod-shaped BoNO single crystal ($5 \times 0.6 \times 0.3$ mm) placed in a two-axis goniometer probe [39] with the longest dimension along the coil axis. NMR data were collected using an Apollo Tecmag spectrometer, using the $\pi/2 - \tau - \pi$ spin-echo sequence, with an average $\pi/2$ pulse length of $t_{\pi/2} = 0.8$ μ s.

III. RESULTS AND DISCUSSION

A. Structure and DFT calculations

The BoNO crystallographic data are summarized in Table I. The core molecular structure consists of two

TABLE I. Summary of BoNO's crystallographic data measured at $T = 100$ and 300 K in a dry nitrogen current.

		BoNO	
Formula unit (f.u.)	C ₂₀ H ₂₅ N ₃ O ₄		
Crystal system	orthorhombic		
Space group	No. 61 <i>Pbca</i>		
Point group	<i>mmm</i>		
F.u. in unit cell (<i>Z</i>)	8		
Radiation source	Mo K $_{\alpha}$		
Temperature (K)	100	300	
<i>a</i> (Å)	10.57900(5)	10.7682(2)	
<i>b</i> (Å)	31.50380(12)	31.6111(8)	
<i>c</i> (Å)	11.68320(5)	11.7298(3)	
$\rho_{\text{calc.}}$ (g cm ⁻³)	1.267	1.236	
Used/total reflections	3147/4223	3515/4262	
$R[I > 2\sigma(I)]$	0.0924	0.0556	
Goodness of fit	1.329	1.051	

metapositioned aminoxyl groups (Fig. 1), forming a ferromagnetic coupling unit [30]. The introduction of additional functional groups improves molecular stability and facilitates the formation of macroscopic single crystals.

The introduced polar $-\text{NO}_2$ substituent aids the formation of a desired one-dimensional geometry due to the electrostatic interaction between the neighboring molecules. In the observed molecular chains, running along the crystallographic *a* axis, electron-rich aromatic 3,5-bis(*N*-*tert*-butylaminoxyl)benzene moieties make an angle of $\approx \pm 45^\circ$ to the *a* axis [Fig. 1(b)]. The stacked BoNO molecules are separated by $\mathbf{a}/2$ along the chain, and $\pm \mathbf{b}$ and $\pm \mathbf{b}/2 \pm \mathbf{c}/4$ between neighboring chains ($z = 6$) in a distorted triangular (hexagonal) configuration, hence reducing frustration (Fig. 2). Each unit cell consists of eight BoNO molecules, forming four parallel chains along the crystallographic *a* axis. *Ab initio* molecular orbital calculations for a single molecule, and DFT calculations for the unit cell, show that the $S = 1$ spin density is primarily distributed between the two aminoxyl groups, with a significant overlap along the chain. The intramolecular coupling was calculated to be $|J_{\text{FM}}|/k_B \approx 450$ K, therefore substantially above room temperature.

Figure 2 shows the intrachain exchange coupling $J_{1\text{D}}$, which results from the direct overlap between the $S = 1$ orbitals of nearest-neighboring BoNO molecules stacked along the *a* axis. In contrast, the interchain $J_{3\text{D}}$ coupling is considerably smaller due to strong localization within C-H bonds in the large *tert*-butyl group, which hinders the transferred exchange coupling between the neighboring chains. Considering only the nearest-neighbor interchain coupling, from the crystal structure we can distinguish three different coupling constants, $J_{3\text{D}}^{(i)}$ ($i = 1, 2, 3$), which are located within the *bc* plane. Unfortunately, it was not possible to accurately calculate the size of $J_{3\text{D}}^{(i)}$ because the basic unit cell is quite large (416 atoms) and such calculations would require substantial computing power. Nevertheless, we can state that our low-resolution calculation gave the average value $zJ_{3\text{D}}/J_{1\text{D}} \approx 0.02$.

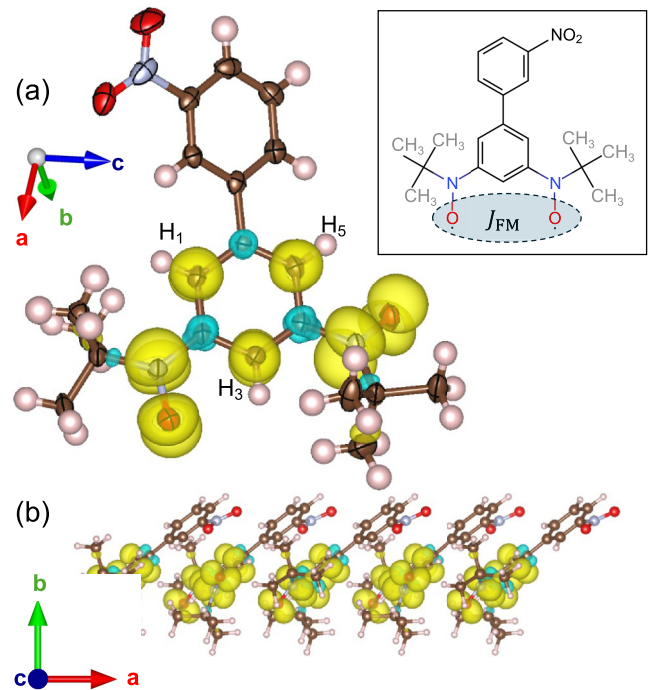


FIG. 1. (a) Molecular structure of BoNO. Atomic positions are determined by the high-resolution x-ray diffraction with 50% thermal displacement ellipsoids shown for nonhydrogen atoms: brown (C), pink (H), red (O), and white (N). The positions of hydrogen atoms are determined by universal force field molecular optimization, consistent with nonhydrogen atomic positions isolated from x-ray data ($E_{\text{min.}} = 463.37$ kJ/mol). The yellow and blue shapes correspond to the positive and negative spin densities, with a cutoff value of $3 \times 10^{-3} e \text{ Bohr}^{-3}$. Crystallographic sites denoted as H_1 , H_3 , and H_5 possess considerable nuclear hyperfine shifts, making them excellent candidates for an NMR study. Inset: The molecular structure of BoNO; the ferromagnetic coupling unit is emphasized by the shaded dashed oval. (b) The stacking of the BoNO molecules to form a chain along the crystallographic *a* axis. VESTA 3 has been used for crystal structure visualization [40].

B. Static susceptibility

The temperature-dependent static magnetic susceptibility (χ) curves measured under an external applied magnetic field of 0.1 T both parallel (*a* axis) and perpendicular (*b* and *c* axis) to the chain direction are shown in Fig. 3. For all orientations, data show almost identical behavior, namely, a Curie-Weiss-like behavior at high temperatures with a pronounced, broad maximum at $T \approx 11$ K, characteristic for low-dimensional systems [41] with dominant antiferromagnetic interactions. The subsequent decrease in $\chi(T)$ is in line with an $S = 1$ antiferromagnetic chain model, where magnetic susceptibility vanishes at $T = 0$ K with the gapped singlet ground state. The measured magnetic moment $\mu_{\text{meas.}} = (2.7 \pm 0.1) \mu_B$ per formula unit (f.u.) is consistent with the $S = 1$ system ($\mu_{\text{theor.}} = 2.82 \mu_B/\text{f.u.}$) and the Curie-Weiss temperature of $\Theta = -(23 \pm 4)$ K determines the antiferromagnetic nature of the intrachain interactions. The presented values for $\mu_{\text{meas.}}$ and Θ are the average value measured for all three orientations. The low uncertainty depicts the equivalency

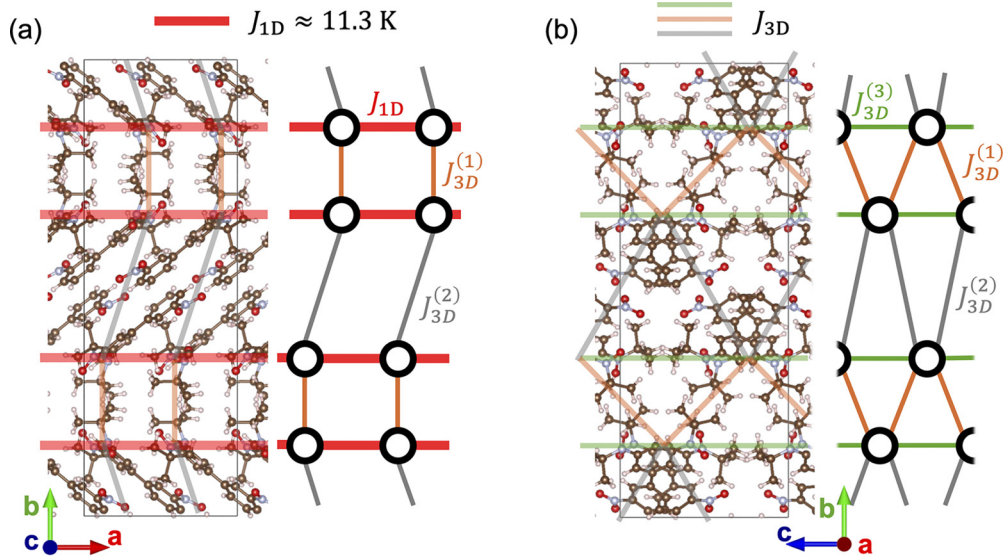


FIG. 2. Single-crystal diffraction reveals a favorable stacking of BoNO molecules which creates a quasi-1D $S = 1$ system. (a) The crystal structure in the ab plane shows chain propagation along the crystallographic a axis, overlaid with the dominant spin-exchange path (red), corresponding to $J_{1D}/k_B \approx 11.3$ K. Weaker interchain couplings, $J_{3D}^{(1)}$ and $J_{3D}^{(2)}$, are indicated by orange and gray lines, respectively. (b) The structure in the bc plane (the chains extend into the page) emphasizes the weaker interchain couplings $J_{3D}^{(i)}$ ($i = 1, 2, 3$) shown by orange, gray and green lines, respectively. Schematic representations of spin-exchange couplings are provided for clarity alongside each crystallographic projection.

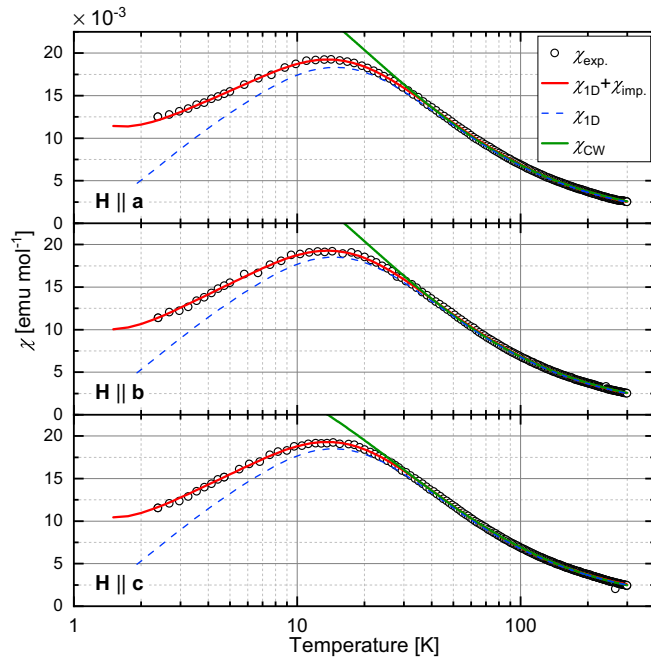


FIG. 3. The low magnetic field measurements of spin susceptibility $\chi(T)$ in $\mu_0 H = 0.1$ T for $\mathbf{H} \parallel \mathbf{a}$ (along the chains) and $\mathbf{H} \parallel \mathbf{b}, \mathbf{c}$ (perpendicular to the chains) display a characteristic maximum consistent with a Haldane system with spin-exchange constant $J_{1D}/k_B = (11.3 \pm 0.1)$ K. The open circles are measured data, and the full red and dashed blue lines are fits to expression (1) (Ref. [42]), with and without the impurity contributions, respectively, in a wide temperature range. Note that in the impurity-free susceptibility (dashed blue), the maximum value is shifted to ≈ 15 K. Curie-Weiss-like behavior (green line) is observed down to $T \approx 30$ K.

of the measured curves, which shows that within the experimental error, the observed magnetic susceptibility is isotropic. A precise determination of antiferromagnetic J_{1D} coupling is done by fitting the closed-form expression derived by Padé approximation of the numerical QMC calculations for an ideal Haldane $S = 1$ model, calculated by Law *et al.* [42]:

$$\chi_{1D}(T) = x\chi^{(\text{imp.})} + (1-x)\mathcal{F}_6\left(\frac{J_{1D}}{k_B T}\right)\chi_C e^{-\Delta/k_B T}, \quad (1)$$

$$\mathcal{F}_n\left(\frac{J_{1D}}{k_B T}\right) = \frac{1 + \sum_{i=1}^n A_i \left(\frac{J_{1D}}{k_B T}\right)^i}{1 + \sum_{i=1}^n B_i \left(\frac{J_{1D}}{k_B T}\right)^i}, \quad (2)$$

where $\chi^{\text{imp.}} = \frac{(g\mu_B)^2 S(S+1)}{3k_B T}$ is the standard 3D Curie susceptibility for unpaired $S = 1$ spins used to model the paramagnetic impurity contribution, x is the impurity concentration, J_{1D} is the intrachain interaction, the Haldane gap is given by $\Delta = 0.411J_{1D}$, and A_i and B_j represent Padé coefficients in the susceptibility expression for the $S = 1$ system [43]. The paramagnetic impurity contribution is minute, $x = (1.4 \pm 0.2)\%$, and can easily account for the slower reduction of susceptibility at low temperatures. The dominant chain term in Eq. (1) reduces to the paramagnetic Curie susceptibility in the high-temperature limit, and the exponential term models the singlet-triplet gap. By removing the impurity contribution, the maximum in susceptibility slightly shifts to ≈ 15 K. The fits to the experimental data yield an average value of $J_{1D}/k_B = (11.3 \pm 0.1)$ K for all three orientations. This corresponds to the theoretical gap value of $\Delta/k_B = (4.6 \pm 0.4)$ K. In reality, the gap is reduced by the presence of weak 3D interactions [20], as well as in the case of monoradical and paramagnetic impurities present in the sample [25].

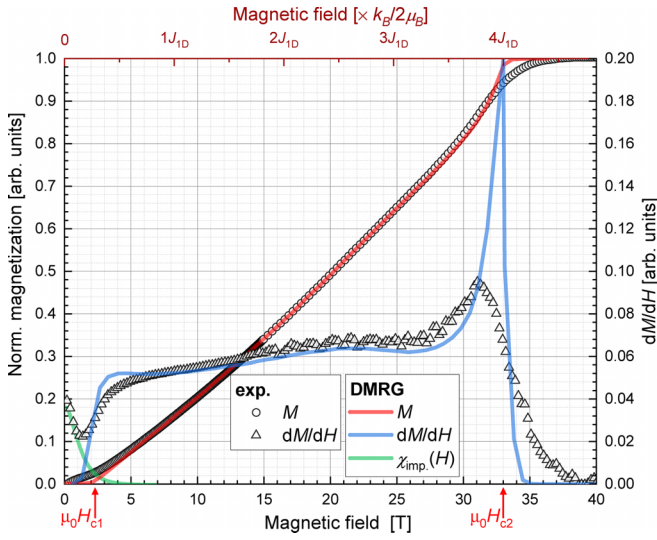


FIG. 4. The high-field magnetization (black circles) measured at $T = 1.3$ K, in pulsed magnetic fields up to $\mu_0 H = 40$ T, agree well with the DMRG calculation of a prototypical Haldane system (red line) of tetragonal symmetry from [45], for $zJ_{3D}/J_{1D} = 0.04$. Additionally, experimental (triangles) and theoretical (blue line) data for dM/dH also show a good agreement. The visible upturn in the dM/dH data at low magnetic fields arises from the paramagnetic impurities ($<1\%$) in the sample, modeled using the $S = 1$ Brillouin function (green line).

Following the study of the thermodynamic properties of the $S = 1$ chain [41], from the J_{1D} value one can expect that the vanishing susceptibility is expected only at temperatures below 1 K.

The high-temperature values of susceptibility were analyzed (Appendix A) to determine the intramolecular coupling value $|J_{FM}|$, and we find the data consistent with $|J_{FM}|/k_B \gtrsim 500$ K, in good agreement with the DFT result.

We can also include the effect of interchain interactions using a standard [44] mean-field correction, $\chi_{3D} = \chi_{1D}/[1 - (zJ_{3D}/N_A g^2 \mu_B^2) \chi_{1D}]$, where χ_{1D} , N_A , and μ_B are the theoretical $S = 1$ chain susceptibility modeled using the expression (1), Avogadro's constant, and Bohr magneton, respectively. The relative scale of zJ_{3D}/J_{1D} makes it difficult to fit the absolute value of zJ_{3D} in the paramagnetic phase. Nevertheless, the data conservatively suggest that the total interchain coupling $zJ_{3D}/k_B \approx 0.6$ K is almost two orders of magnitude smaller than J_{1D} .

C. High-field magnetization

The high-field magnetization measurement at a temperature of $T = 1.3$ K is shown in Fig. 4. We compare our magnetization and susceptibility data to a density-matrix renormalization group (DMRG) calculation from Ref. [45] that was done for a $S = 1$ chain with $zJ_{3D}/J_{1D} = 0.04$ (with $z = 4$). As can be seen, the DMRG result matches the experiment. It should be noted, however, that the exact value of the zJ_{3D}/J_{1D} can be retrieved only once the values of H_{c1} and H_{c2} at $T = 0$ K are determined. The H_{c1} (H_{c2}) value at 0 K is lower (higher) than that seen in Fig. 4, but nevertheless it gives us a good estimate of total interchain coupling. The magne-

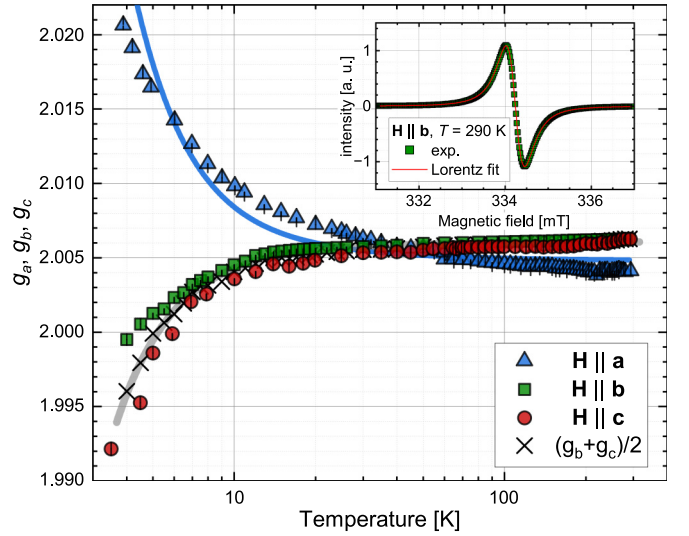


FIG. 5. The values of g_a , g_b , and g_c extracted from the line-shape fits of the X-band EPR spectra are plotted in a wide temperature range from 300 to 3.5 K. The observed temperature dependence is successfully accounted for using the Nagata *et al.* model [47,48] (blue and gray lines). Crosses mark the average values of the g factor measured perpendicular to the chains ($g_b + g_c$)/2 for easier comparison to the model. Below 10 K, the system is no longer a paramagnet and deviations from the model are expected. Inset: The EPR line measured for $\mathbf{H} \parallel \mathbf{b}$ at 290 K and the corresponding Lorentz fit.

tization curve displays a characteristic behavior at the lower critical field $\mu_0 H_{c1} \approx 2$ T, while close to the upper critical field $\mu_0 H_{c2} \approx 33$ T, the field dependence is smeared due to the finite-temperature effects. At intermediate magnetic fields, the increase in magnetization, $M(H)$, is quasilinear before reaching complete polarization [46]. Although comparison to the theoretical curve is not a fit, the used $zJ_{3D}/J_{1D} = 0.04$ value is consistent with our mean-field result of 0.053 obtained from dc susceptibility.

The measured H_{c1} (H_{c2}) values indicate that in this Haldane system, the entire field-induced phase diagram can be thoroughly studied, which is not possible in known Haldane systems with low magnetic anisotropy.

D. Electron paramagnetic resonance

X-band electron paramagnetic resonance (EPR) measurements are used to confirm the (nearly) isotropic spin Hamiltonian of the BoNO molecule (Fig. 5). The single-crystal EPR spectra were measured at room temperature for the magnetic field oriented parallel and perpendicular to the chain direction. A single narrow EPR spectral line (Fig. 5, inset) is observed for each orientation and Lorentzian fits to the data give $g_a = 2.0041$ and $\mu_0 \Delta H_a = 2.99$ mT for the field along the chains, and $g_b = 2.0065$, $\mu_0 \Delta H_b = 0.75$ mT, $g_c = 2.0063$, and $\mu_0 \Delta H_c = 0.89$ mT for the fields perpendicular to the chain direction. Remarkably, small g factor deviations from the free electron value $g_e = 2.00232$ and narrow linewidths are consistent with the light-element nature of BoNO molecules where spin-orbit coupling and the resulting magnetic anisotropic Hamiltonian terms are very small.

Temperature dependence of the g factor is most pronounced at low temperatures, where the g factor change reaches about $|\Delta g| = 0.015$. The change is positive for the magnetic field aligned along the chain a axis, while it is negative for the other two orientations (Fig. 5). This known effect is expected to arise from emerging short-range fluctuations along the chains, which shift the EPR spectral line [49–52]. We used a nearest-neighbor (NN) uniaxial Heisenberg chain model in a paramagnetic state developed by Nagata *et al.* [47,48] to quantitatively address the temperature dependencies of the effective g factors,

$$g_{\parallel}^{\text{eff.}}(T) = g_{\parallel} + \frac{6\alpha g_{\parallel}}{10x(T)} \left[\frac{2 + u(T)x(T)}{2 - u(T)^2} - \frac{2}{3x(T)} \right], \quad (3)$$

$$g_{\perp}^{\text{eff.}}(T) = g_{\perp} - \frac{3\alpha g_{\perp}}{10x(T)} \left[\frac{2 + u(T)x(T)}{2 - u(T)^2} - \frac{2}{3x(T)} \right], \quad (4)$$

where $g_{\parallel}^{\text{eff.}}$ and $g_{\perp}^{\text{eff.}}$ stand for the temperature-dependent effective g factors measured for the magnetic field along and perpendicular to the chains, respectively. The parameter $u(T) = \coth[1/x(T)] - x(T)$, where $1/x(T) = J_{1D}S(S+1)/k_B T$ is related to the spin correlation function, and $\alpha = -\mu_0 g^2 \mu_B^2 / (4\pi J_{1D} r_{\text{NN}}^3)$ models the dipolar magnetic interaction between $S = 1$ sites separated by r_{NN} along the chain. Since our spin-chain environment is not uniaxial, we compare the $g_{\perp}^{\text{eff.}}(T)$ dependence to the average g factor perpendicular to the chains, $(g_b + g_c)/2$. By using the previously determined J_{1D} , g_{\parallel} and g_{\perp} , and α as the only free parameter, the model fits our data (Fig. 5) for $\alpha = 1.7 \times 10^{-4}$, i.e., $r_{\text{NN}} = 11 \text{ \AA}$. Some deviations are visible in $g_a(T)$ for $k_B T \lesssim J_{1D}$, but this is expected since there the quantum effects become dominant while the model is classical in nature. The fitted r_{NN} value is larger than the mean intrachain distance between molecules ($\approx 5 \text{ \AA}$); however, this can be explained by the simplicity of the model—in reality, dipolar contribution has a longer range than only NN, and in BoNO the spin-wave function is distributed via several atoms of the molecule, which is unaccounted for by the model.

The presence of short-range fluctuations for $k_B T \leq J_{1D}$ is further corroborated by the temperature dependence of the fitted linewidths ΔH (Fig. 6), which we model using the expression

$$\Delta H(T) = \Delta H_0 + a \frac{\tau_c}{1 + (\omega_{\text{EPR}} \tau_c)^2} + b T^{-\gamma}. \quad (5)$$

In addition to the temperature-independent intrinsic linewidth ΔH_0 , the observed high-temperature maximum at $T = 150 \text{ K}$ is treated using a Bloembergen-Purcell-Pound (BPP) type of relaxation mechanism with a well-defined frequency of the local magnetic field fluctuations, and the last term describes short-range correlations [50,53] characterized by a power-law exponent γ . The BPP-modeled fluctuations are probably the result of the molecular librations and rotations defined by the energy scale E_a and characteristic correlation time τ_c , transferred via intramolecular dipolar coupling between $S = 1$ spins and the nearby hydrogen magnetic moments. We can exclude any structural transition since the

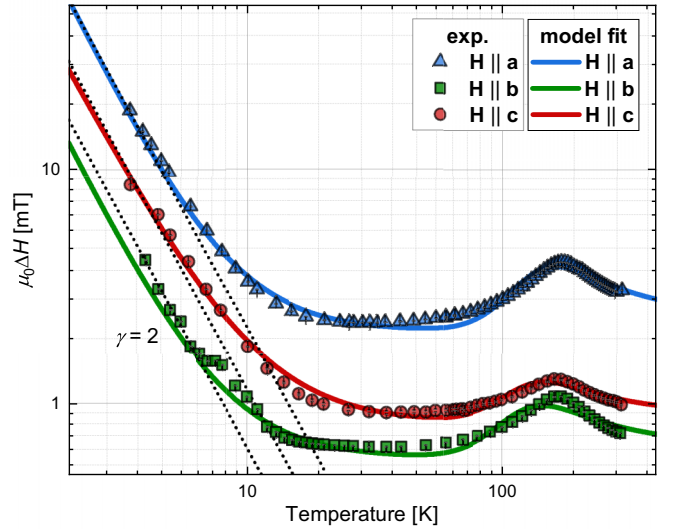


FIG. 6. Temperature dependence of the X-band EPR linewidth ΔH for the magnetic field along the chain direction (a axis, triangles) and perpendicular to it (b and c axes, squares and circles, respectively). The data show a good agreement with the proposed model (5) with both BPP and power-law terms. Dotted black lines illustrate $\propto T^{-2}$ behavior observed in systems with short-range correlations.

crystal structure measured at 300 and 100 K revealed only a contraction of the unit cell. The BPP correlation time τ_c is usually a thermally activated term, $\tau_c = \tau_{\infty} \exp(E_a/k_B T)$. The extremal relaxation rate is expected for $\omega_{\text{EPR}} \tau_c = 1$, where the observed linewidth is maximal, with ω_{EPR} as the measurement frequency. The pronounced low-temperature broadening that we identify as short-range order effects gives a characteristic power-law behavior with exponent γ . The fitted curves yield $\tau_{\infty} = 7.5 \times 10^{-13} \text{ s}$, $E_a/k_B = 575 \text{ K}$, and $\gamma = 2.2$. The magnitude of the fitted activation energy ($E_a = 4.2 \text{ kJ/mol}$) matches the expected range for the energy barriers between different molecular conformations [54]. The low-temperature increase of $\Delta H(T)$ approximately follows T^{-2} power-law dependence, which is usually associated with the short-range correlations in quantum spin systems with the staggered field.

We complement our dc susceptibility data with the measurements of EPR susceptibility (Fig. 7) at the external magnetic field of $\mu_0 H = 334 \text{ mT}$. The data follow a Curie-Weiss dependence down to a maximum value at $\approx 15 \text{ K}$, and it is suppressed on further cooling due to the singlet-triplet gap. In the figure, we compare the measured EPR susceptibility to the impurity-free data of Fig. 3. As can be seen, the datasets match each other, confirming the validity of the Curie-term subtraction.

Finally, we discuss the angular dependence of the EPR spectra taken at $T = 300 \text{ K}$, shown in Fig. 8. In the upper panels, we plot the g factors against the angle measured away from the chain direction in the crystal ac plane (left panel) and in the bc plane that is perpendicular to the chains (right panel). The data show that the g factor is almost angle independent in the plane perpendicular to the chain direction. The main angular dependence is thus with respect to the angle from the chain direction. The fits to the angular dependencies are

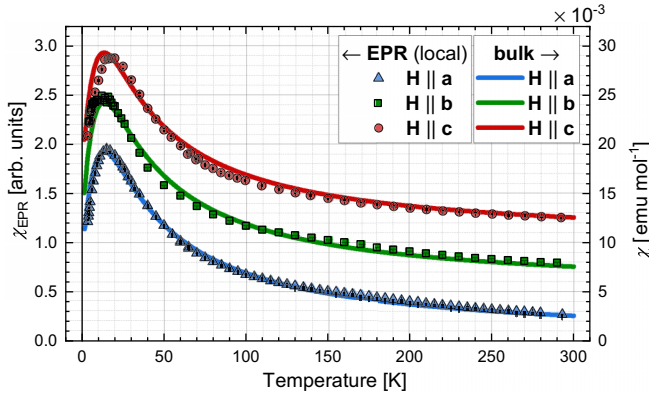


FIG. 7. The EPR susceptibility data at $\mu_0 H = 334$ mT, obtained by a double integration of the derivative of the EPR spectrum (inset of Fig. 5), are compared to the corresponding bulk measurements [each dataset is offset by 0.5 (arb. units), i.e., 0.005 emu/mol, for clarity].

generated by a simple projection of the diagonal g tensor, with principle values corresponding to the previously determined g_a , g_b , and g_c values.

The angular dependence of the EPR linewidth, shown in the lower panel of Fig. 8, holds the information about the magnetic anisotropy. For the field rotation in the ac plane, the linewidth ΔH shows a minimum value at $\varphi \approx 50^\circ$ and maximum for the field along the chain direction—a characteristic behavior of quasi-1D antiferromagnets [55]. As the spin-orbit coupling is very weak, we can assume that the main magnetic anisotropy is the dipolar interaction between neigh-

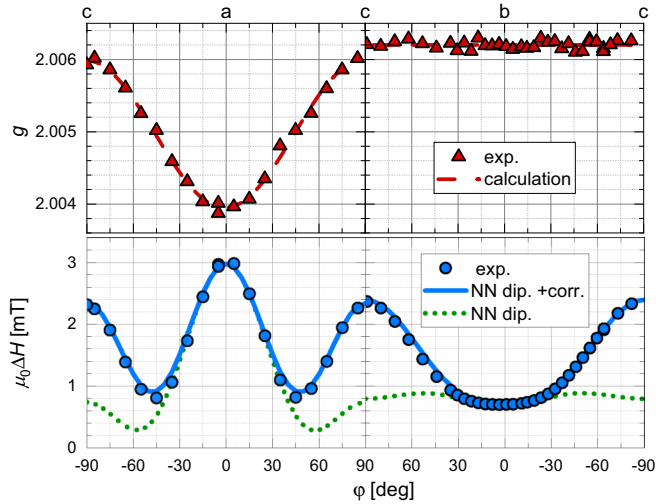


FIG. 8. The angular dependence of the g factor and linewidth ΔH values taken along the $c - a - c - b - c$ path. The change in g factor is attributed to a small molecular orbital anisotropy, while ΔH values are explained by the nearest-neighbor dipolar interaction between $S = 1$ coupled units. The red dashed line is calculated by rotating the g tensor, using the previously determined g_a , g_b , and g_c values. The green dotted lines represent the calculated NN dipolar broadening and the magnitude is corrected when small intramolecular interactions between $S = 1/2$ spins are taken into account (full lines).

boring $S = 1$ molecular sites. The change in EPR linewidth due to the magnetic dipolar interactions can be calculated in the exchange narrowing limit,

$$\Delta H = C \frac{M_2^{\text{dip.}}}{J_{\text{ID}}}, \quad (6)$$

where $M_2^{\text{dip.}}$ is the second moment of the resonance due to the dipolar interactions, and line-shape-dependent constant C ranges between 1 and 2 in similar systems [56,57]. In the point-spin model where the effective spin $S = 1$ is centered between the radical NO groups, the $M_2^{\text{dip.}}$ is easily calculated,

$$M_2^{\text{dip.}} = \frac{3}{4} S(S+1) \frac{\mu_0^2 \mu_B^4 g^4}{(4\pi)^2} \sum_{i \in \text{NN}} \frac{(3 \cos^2 \Theta_i - 1)^2}{r_i^6}, \quad (7)$$

where Θ_i is the angle between the external magnetic field and the vector $\mathbf{r}_i = r_i \hat{\mathbf{r}}_i$ that connects $S = 1$ sites of the neighboring molecules. The sum converges rapidly due to the $1/r_i^6$ term, so only the nearest neighbors have to be accounted for. The calculated ΔH with $C = 1.6$ and $J_{\text{ID}}/k_B = 11.3$ K qualitatively explains the observed data, as is shown by the dotted line in the lower panel of Fig. 8, even with such a simple approach. Reproducing the exact ΔH angle dependence quantitatively is challenging since there may be other contributing factors too [58]. In our case, ΔH is further affected by the on-site (anisotropic) distribution of the molecular orbital, which requires substantial computer power to take into account. Since spin-orbit coupling is, for such a light-element molecular system, expected to be small, the single-ion anisotropy should be negligible in BoNO. Yet, an extra term can still arise due to the intramolecular interaction of two $S = 1/2$ spins forming the single $S = 1$ unit. Therefore, in the last step of our analysis, we add the $A \sin^4 \varphi$ term in addition to the dipolar contributions from Eqs. (6) and (7). A good agreement to our data is finally obtained with $A = 1.6$ mT.

E. Nuclear magnetic resonance

The nuclear magnetic resonance (NMR) spectral and relaxation measurements have previously been frequently used in studies of similar compounds to confirm and progressively improve the theoretical description of phenomena in low-dimensional quantum magnets [7,15,59–62]. The hydrogen (^1H) spectrum can be modeled by a simple spin $I = 1/2$ NMR Hamiltonian,

$$\mathcal{H} = \gamma \mathbf{I} \cdot (\mathbf{1} + \mathbf{K}) \mathbf{B}, \quad (8)$$

where $\gamma/2\pi = 42.5774$ MHz/T is the corresponding gyromagnetic constant, \mathbf{I} is the nuclear spin operator, $\mathbf{B} = \mu_0 \mathbf{H}$ is the external magnetic field, and \mathbf{K} is the nuclear shift tensor. The spectral line observed at a given frequency, $f_{\text{NMR}} = \gamma |\mathbf{B}| \{1 + K(\theta, \phi)\}$, has a frequency shift $K(\theta, \phi)$ correlated to the respective site properties and the external magnetic field orientation defined by the spherical angles (θ, ϕ) , where $\theta = 0^\circ$, $\phi = 0^\circ$ corresponds to the magnetic field aligned with the sample's crystallographic c axis. The $I = 1/2$ NMR

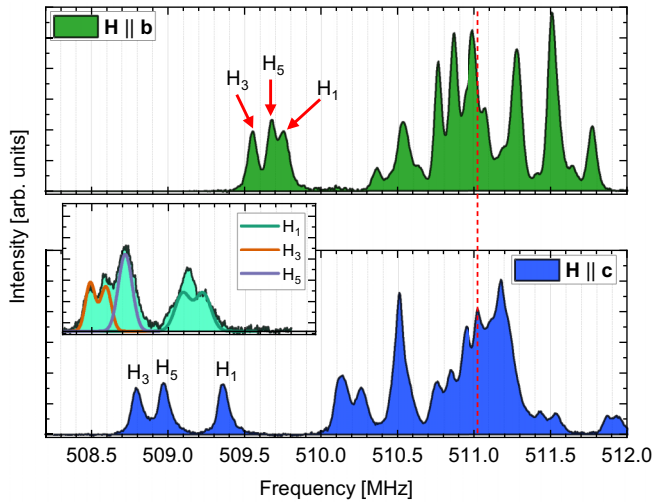


FIG. 9. The frequency-swept ^1H NMR spectra of BoNO single crystal at $\mu_0 H = 12.002$ T, along the crystalline b and c axes, are shown in the upper and lower panel, respectively. The spectra are measured at 25 K. Most of the spectrum is concentrated close to $f_0 = 511.033$ MHz (red dashed line) and cannot be resolved and assigned to the respective ^1H atoms. However, we have successfully assigned the spectral lines with the strongest hyperfine nuclear shifts to the H_1 , H_3 , and H_5 crystallographic positions, respectively. These sites create three lines for $\mathbf{H} \parallel \mathbf{b}$ and $\mathbf{H} \parallel \mathbf{c}$, but split for \mathbf{H} away from crystallographic axes, as seen in the inset. Besides the measured NMR spectrum, the inset also shows the calculated positions corresponding to these sites (see the main text).

Hamiltonian is coordinate inversion symmetric and, consequently, for an arbitrary magnetic field direction, four spectral lines are expected for *each* crystallographic ^1H site within the $Pbca$ unit cell. However, fewer spectral lines will be observed for the magnetic field directions along the crystal symmetry axes.

The ^1H NMR spectrum of BoNO at $\mu_0 H = 12.002$ T in the paramagnetic phase for magnetic field orientations along the high-symmetry crystal axes $\mathbf{H} \parallel \mathbf{b}$ and $\mathbf{H} \parallel \mathbf{c}$ are displayed in the upper and lower panel of Fig. 9, respectively. Here, due to the strong electron-rich character of the aromatic rings, several ^1H spectral lines are strongly shifted from the bare nucleus Larmor frequency $f_0 = \gamma B$. The ^1H NMR spectrum has two contrasting features: a set of high-intensity spectral lines spanning a relatively wide frequency range close to the bare nucleus frequency $f_0 = 511.033$ MHz that correspond to ^1H sites with small shifts, and a region of well-defined spectral lines with considerable negative frequency shifts (marked in Fig. 9 as H_1 , H_3 , and H_5). As mentioned earlier, for the magnetic field along the b and c axes, there are only three lines corresponding to the H_1 , H_3 , and H_5 sites, and when the sample is oriented away from the axes, the lines split (inset of Fig. 9). The lines are assigned to the corresponding ^1H sites shown in Fig. 1, through a procedure which we will elaborate on later. Although some of the high-intensity lines close to f_0 can be clearly distinguished, the frequent overlapping during the sample rotation in an external magnetic field or temperature dependence severely hinders the possibility of spectral line assignment. Furthermore, we argue that spectral

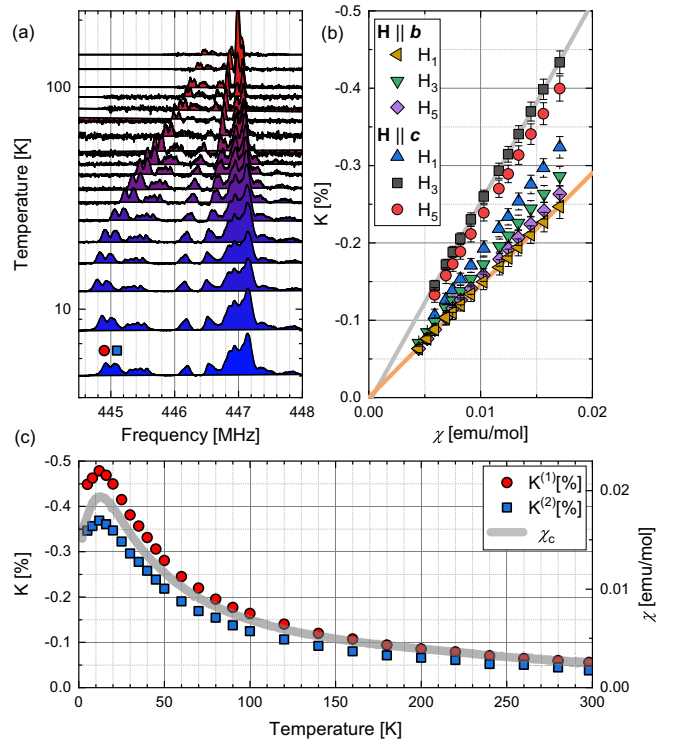


FIG. 10. (a) The temperature dependence of the NMR spectra for $\mu_0 H = 10.5$ T, oriented at $\angle(H, c) = 45^\circ$ where the observed frequency shift is the largest. (b) The $K - \chi$ plot for H_1 , H_3 , and H_5 protons, with $\mathbf{H} \parallel \mathbf{b}$, $\mathbf{H} \parallel \mathbf{c}$, reveals negligible orbital contribution. (c) The spectra are overlaid with the scaled bulk susceptibility, represented by a thick gray line.

lines close to f_0 are only marginally influenced by the $S = 1$ system, so we will focus our analysis on the set of lines with large hyperfine shifts.

The temperature dependence of the NMR spectra has been measured in a paramagnetic phase in an external field of $\mu_0 H = 10.5$ T with the field at an angle $\angle(H, c) = 45^\circ$ from the c to b axis [shown in Fig. 10(a)], where the H_1 , H_3 , and H_5 spectrum spans the broadest frequency range. At this orientation, the spectrum becomes progressively wider as the temperature is lowered, down to the temperature $T = 16$ K, where the maximal frequency shift is observed. The measurements were also done for $\mathbf{H} \parallel \mathbf{b}$ and $\mathbf{H} \parallel \mathbf{c}$, but we do not show these spectra here for clarity and brevity of the presentation. The paramagnetic NMR frequency shift reflects the bulk susceptibility of the sample scaled to each spectral line and, through the $K - \chi$ plot [Fig. 10(b)], this relation can be used to determine the diagonal components of the shift tensor. The figure also shows that there is no anomalous behavior of K in the entire paramagnetic temperature region, notably close to the BPP behavior seen by EPR (Fig. 6). Although no structural change has been seen by x-ray diffraction, since it is not sensitive to hydrogen positions, we wanted to corroborate it by characterizing ^1H NMR spectra. To show the $K(T)$ dependence in more detail, we selected the ^1H lines with the largest hyperfine coupling, i.e., the largest NMR shift [marked by symbols in Fig. 10(a)], and plot the corresponding $K(T)$ dependence in Fig. 10(c). The data follow the susceptibility

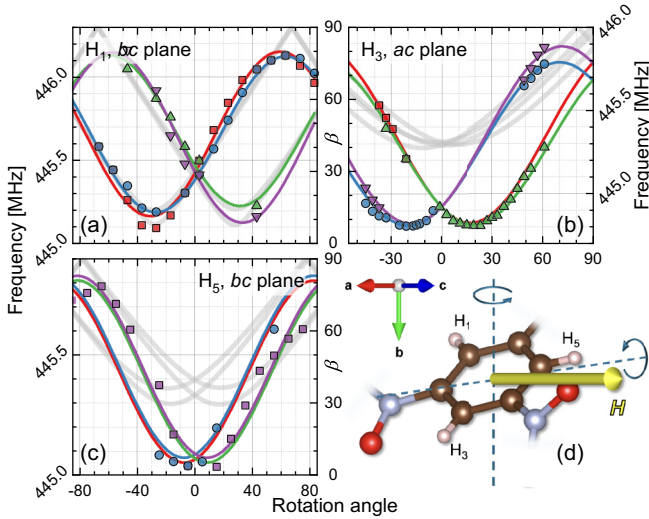


FIG. 11. (a)–(c) Rotational positions of H_1 , H_3 , and H_5 NMR lines (separate panels used for clarity) in the paramagnetic phase at $T = 20$ K, with \mathbf{K} -tensor fits for each site. When the magnetic field is rotated in the plane of symmetry (ac or bc), only two lines are visible; however, a small initial misalignment splits the spectra, revealing four lines for each site. Gray lines illustrate the rotational dependence of β : an angle between the C_i - H_i bonds and the magnetic field \mathbf{H} . (d) A schematic of the rotations is presented, together with the magnified view of the aromatic ring that connects the three hydrogen sites. There are eight BoNO molecules in a unit cell, which gives four different orientations of the corresponding aromatic rings (Fig. 2).

curve, which confirms that the EPR line broadening with a maximum at $T = 150$ K is a dynamical effect accounted for by Eq. (5) and not related to the crystal structure.

A rigorous treatment of the NMR spectra and a precise determination the \mathbf{K} shift tensor for multiple ^1H sites is essential for the study of the microscopic properties of the system. Here, we have performed a set of NMR spectral measurements at $T = 20$ K, $H = 10.5$ T for different magnetic field orientations in ac and bc planes [Figs. 11(a)–11(c)]. The positions of the spectral lines were fit with the Gaussian line shape and subsequently fitted to expression for f_{NMR} . Quite generally,

the \mathbf{K} tensor can be expressed by the following equation [63]:

$$\mathbf{K} = -4\pi\mathbf{N}\frac{\chi}{N_A v} + \mathbf{K}_{\text{tr.}} + \mathbf{K}_{\text{dip.}}, \quad (9)$$

where $\mathbf{N} = (0.038, 0.336, 0.626)$ stands for a diagonal demagnetization tensor calculated for a rectangular sample shape [64] with molar volume v . $\mathbf{K}_{\text{tr.}}$ and $\mathbf{K}_{\text{dip.}}$ are \mathbf{K} -tensor components due to transferred and dipolar hyperfine interactions. $\mathbf{K}_{\text{tr.}} = \mathbb{A}_{\text{tr.}}\chi/N_A\mu_B$, where $\mathbb{A}_{\text{tr.}}$ is the transferred hyperfine coupling tensor, while $\mathbf{K}_{\text{dip.}} = \mathbb{D}\chi/N_A\mu_B$, where \mathbb{D} is the dipolar hyperfine coupling tensor. \mathbb{D} is easily calculated as

$$\mathbb{D} = \sum_i \frac{\mu_0 g \mu_B}{4\pi |\mathbf{r}_i|^3} \begin{pmatrix} 3x_i^2 - 1 & 3x_i y_i & 3x_i z_i \\ 3x_i y_i & 3y_i^2 - 1 & 3y_i z_i \\ 3x_i z_i & 3y_i z_i & 3z_i^2 - 1 \end{pmatrix}, \quad (10)$$

where $\mathbf{r}_i = (x_i, y_i, z_i)$ is a position vector of a $S = 1$ magnetic moment with respect to the ^1H nucleus given in Cartesian coordinates. The sum goes over multiple unit cells until convergence is reached. In the case of BoNO, \mathbb{D} is calculated by considering delocalized $S = 1$ positions and weight averaging their contributions using a DFT-calculated probability density function with a chosen convergence radius $r_c = 100$ Å. Due to the $1/r^3$ dependence of a dipolar coupling, convergence is rapidly reached within $r \approx 30$ Å. The demagnetization effects \mathbf{N} are usually neglected in paramagnetic compounds; however, in highly asymmetric rod-shaped crystals, the contribution to the external field is of the order of the observed NMR shifts ($\approx 0.1\%$). Similarly, the transferred hyperfine coupling should be negligible in a covalently bonded system with a strong electron localization, but we argue that in BoNO, the nature of delocalized orbitals induces a significant coupling between the ^1H site and the electron spins formally placed on NO molecular groups. The fitted values of the \mathbf{K} tensor for the H_1 , H_3 , and H_5 positions are summarized in Table II. Indeed, as can be seen, the demagnetization and dipolar coupling alone cannot adequately explain the observed NMR frequency shifts and rotational dependence. By subtracting the dipolar and demagnetization components, we show that the NMR shift is dominantly affected by the transferred hyperfine coupling mediated by the delocalized π orbital of the aromatic ring.

TABLE II. Nuclear magnetic shift tensors (in %) for the assigned ^1H spectral lines. The shift tensor is dominated by the large diagonal elements, visually separated by a single line from the smaller, off-diagonal elements, which are noticeably changed by the dipolar and demagnetizing contributions.

Component	Site H_1			Site H_3			Site H_5		
	\mathbf{K}	$\mathbf{K}_{\text{dip.}}$	$\mathbf{K}_{\text{tr.}}$	\mathbf{K}	$\mathbf{K}_{\text{dip.}}$	$\mathbf{K}_{\text{tr.}}$	\mathbf{K}	$\mathbf{K}_{\text{dip.}}$	$\mathbf{K}_{\text{tr.}}$
xx	-3.952	0.049	-3.998	-3.011	0.229	-3.237	-8.314	0.105	-8.416
yy	-2.677	0.004	-2.653	-4.265	0.050	-4.287	-2.997	-0.059	-2.91
zz	-3.866	-0.053	-3.762	-5.177	-0.279	-4.848	-4.658	-0.045	-4.561
yz	-0.960	-0.030	-0.93	0.76	0.064	0.111	-0.250	-0.096	-0.154
xz	0.005	-0.005	0.010	-0.702	-0.028	-0.674	0.	-0.075	0.075
xy	-0.269	0.080	-0.348	-0.488	0.247	-0.734	0.	0.091	-0.091

We continue to the NMR spectrum site assignment. Typically, if the transferred hyperfine coupling were negligible, one could assign NMR lines to specific sites by comparing the behavior of the NMR shifts with rotational dependence of the dipolar term. However, in our case, we resorted to a different approach. It has been shown for a similar molecular environment [65–67] that the largest hyperfine tensor component is dominantly oriented (within $\pm 10^\circ$) along the corresponding C-H bond, while the smallest component is oriented (again, within $\pm 10^\circ$) perpendicular to the aromatic ring. To assign each \mathbf{K} tensor to the correct crystallographic position, we matched the observed rotation dependence of the shift to the rotation dependence of the angle β between each C-H bond and the external magnetic field [gray curves in Figs. 11(a)–11(c)], as depicted for a single molecule in Fig. 11(d). Since the plane formed by the H_1 , H_3 , and H_5 sites is tilted with respect to the rotation planes, for selected rotations, the magnetic field will never be completely along the C-H bond; however, as the sample rotates, the angle β will reach its minimum position (corresponding to the largest frequency shift) and, approximately 90° away from that position (the exact angle depends on the precise orientation of the C-H bond), the C-H bond will be perpendicular to the magnetic field. As shown, each rotational dependence of the shift consistently follows the rotational dependence of the angle β , with almost matching minimal and maximal values. It should be kept in mind that in Fig. 11(d), for clarity, we show only one aromatic ring from the unit cell, for which one can observe one of the presented curves in Figs. 11(a)–11(c). The other three curves are created by other symmetry-related H_1 , H_3 , and H_5 sites in the unit cell.

IV. CONCLUSION

In this work, we have presented an organic compound 3,5-bis(*N-tert*-butylaminoxyl)-3'-nitro-1,1'-biphenyl (abbreviated BoNO) as an ideal candidate for a prototype Haldane system. In BoNO, an $S = 1$ unit is formed by a strong ferromagnetic intramolecular coupling $|J_{\text{FM}}|/k_B \gtrsim 500$ K between electrons from two radical NO molecular groups. We have determined that BoNO crystallizes in an orthorhombic $Pbca$ unit cell with a molecular stacking crucial for a quasi-one-dimensional behavior. The bulk magnetization and EPR measurements in the paramagnetic phase display the Curie-Weiss behavior with the effective moment $\mu_{\text{meas.}} = (2.7 \pm 0.1)\mu_B/\text{f.u.}$ corresponding to the $S = 1$ system. Both measurements feature a maximum in susceptibility at ≈ 15 K, followed by a steep suppression in $\chi(T)$ characteristic of low-dimensional systems. The paramagnetic $\chi(T)$ dependence suggests a dominant antiferromagnetic spin exchange, which can be attributed to $J_{\text{ID}}/k_B = (11.3 \pm 0.1)$ K obtained by fits to Padé approximated QMC data. At the high-temperature end, the fit to the biradical susceptibility model is virtually indistinguishable from a Curie-Weiss law with $S = 1$, proving that the ferromagnetic intramolecular coupling constant is much larger than 300 K. When the bulk magnetization measurements are performed at 1.3 K up to the $\mu_0 H = 40$ T, we observe a quasilinear increase above $\mu_0 H_{c1} \approx 2$ T where

the singlet-triplet gap in the system is closed, and a fully polarized state above $\mu_0 H_{c2} \approx 33$ T. These field values indicate that in this Haldane system, the entire field-induced phase diagram can be thoroughly studied. The EPR measurements also confirm that BoNO has a highly isotropic g tensor in the paramagnetic state with $g_a = 2.0041$, $g_b = 2.0065$, and $g_c = 2.0063$ remarkably close to the free electron value $g_e = 2.0032$. At low temperatures, g_i ($i = a, b, c$) deviate from g_e in accordance with emerging one-dimensional short-range antiferromagnetic correlations. The EPR linewidth changes can be attributed to both dipolar and short-range order effects present in the sample. Finally, we did temperature-dependent ^1H NMR measurements to corroborate the previous findings. We have analyzed the ^1H NMR rotation spectra, assigned specific spectral lines to the crystallographic H_1 , H_3 , and H_5 positions, and determined the magnitude and origin of the nuclear resonance frequency shifts. The presence of ^1H sites which are strongly coupled to the $S = 1$ spin system makes ^1H NMR a valuable technique for the future study of the TLL and BEC physics in the system. In particular, theoretical predictions for the TLL phase in a Haldane chain can now be tested in the entire phase space [68]. Furthermore, the study of emerging excitations [12] at the upper critical field H_{c2} can be extended to a Haldane chain system. Demonstrably, BoNO presents a unique research opportunity as a Haldane system with no apparent spin Hamiltonian anisotropy and a textbook example of properties in a low-dimensional quantum spin system.

ACKNOWLEDGMENTS

We acknowledge fruitful discussions with M. Dupont, N. Laflorencie, S. Capponi, N. Došlić, and P. Sengupta. We thank D. Pajić and D. Barišić for helping us with the susceptibility measurements. M.S.G. and I.J. acknowledge the support of Croatian Science Foundation (HRZZ) under the Grant No. IP-2018-01-2970 and the support of project CeNIKS co-financed by the Croatian Government and the European Union through the European Regional Development Fund - Competitiveness and Cohesion Operational Programme (Grant No. KK.01.1.1.02.0013). This work was partly supported by JSPS KAKENHI Grant No. JP23K25824. M. Herak acknowledges the support of project Cryogenic Centre at the Institute of Physics - KaCIF, co-financed by the Croatian Government and the European Union through the European Regional Development Fund - Competitiveness and Cohesion Operational Programme (Grant No. KK.01.1.1.02.0012) and the support of the project Ground States in Competition – Strong Correlations, Frustration and Disorder – FrustKor financed by the Croatian Government and the European Union through the National Recovery and Resilience Plan 2021-2026 (NPOO).

APPENDIX: ESTIMATING INTRAMOLECULAR COUPLING J_{FM}

The intramolecular coupling J_{FM} in the organic biradicals can be determined from the magnetic susceptibility

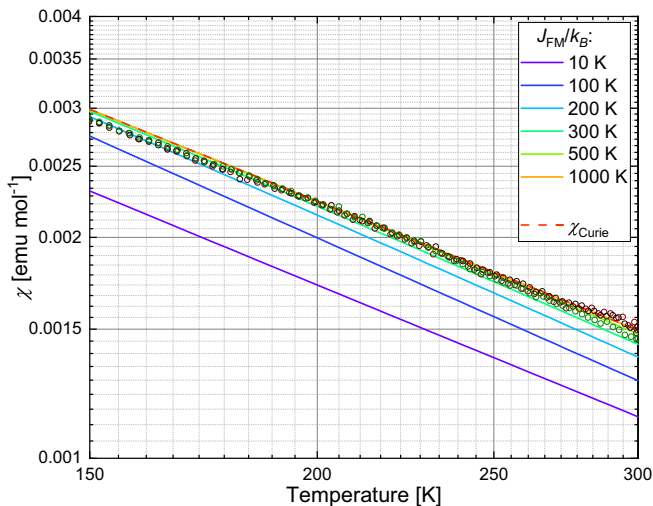


FIG. 12. Comparison of susceptibility values (circles) at temperatures above 150 K to Eq. (A1) for different J_{FM} values and to the Curie temperature dependence from fits in Fig. 3. From the dataset, one can conclude that $|J_{\text{FM}}|/k_B \gtrsim 500$ K.

measurements when $k_B T/|J_{\text{FM}}| \gtrsim 1$ [30],

$$M_{\text{birad}} = 2g\mu_B \left(\frac{\sinh \delta}{1 + 2 \cosh \delta + e^{-2|J_{\text{FM}}|/k_B T}} \right), \quad (\text{A1})$$

where $\delta = g\mu_0\mu_B H/k_B(T - \Theta_{\text{MF}})$, and Θ_{MF} is a mean-field correction for the intermolecular interaction J_{ID} . This general expression reduces to the well-known Bleaney-Bowers equation [69] in low magnetic fields, $g\mu_0\mu_B H \ll k_B T$, or Curie-Weiss behavior in the strong-coupling limit, $|J_{\text{FM}}| \gg k_B T$. As is shown in Fig. 12, it was not possible to distinguish between a Curie-Weiss and M_{birad} for $|J_{\text{FM}}|/k_B \gtrsim 500$ K in our measurements, which leads to the conclusion that in BoNO, intramolecular coupling is much larger than 300 K. This corroborates our DFT calculation result that gave $|J_{\text{FM}}|/k_B \approx 450$ K. In any case, below room temperature, the system can be regarded as an $S = 1$ chain.

- [1] H. Kühne, H.-H. Klauss, S. Grossjohann, W. Brenig, F. J. Litterst, A. P. Reyes, P. L. Kuhns, M. M. Turnbull, and C. P. Landee, Quantum critical dynamics of an $S = \frac{1}{2}$ antiferromagnetic Heisenberg chain studied by ^{13}C NMR spectroscopy, *Phys. Rev. B* **80**, 045110 (2009).
- [2] O. Breunig, M. Garst, A. Klümper, J. Rohrkamp, M. M. Turnbull, and T. Lorenz, Quantum criticality in the spin-1/2 Heisenberg chain system copper pyrazine dinitrate, *Sci. Adv.* **3**, eaao3773 (2017).
- [3] R. Coldea, D. A. Tennant, E. M. Wheeler, E. Wawrzynska, D. Prabhakaran, M. Telling, K. Habicht, P. Smeibidl, and K. Kiefer, Quantum criticality in an Ising chain: Experimental evidence for emergent E_8 symmetry, *Science* **327**, 177 (2010).
- [4] A. W. Kinross, M. Fu, T. J. Munsie, H. A. Dabkowska, G. M. Luke, S. Sachdev, and T. Imai, Evolution of quantum fluctuations near the quantum critical point of the transverse field Ising chain system CoNb_2O_6 , *Phys. Rev. X* **4**, 031008 (2014).
- [5] B. R. Patyal, B. L. Scott, and R. D. Willett, Crystal-structure, magnetic-susceptibility, and EPR studies of bis(piperidinium)tetrabromocuprate(II): A novel monomer system showing spin diffusion, *Phys. Rev. B* **41**, 1657 (1990).
- [6] B. C. Watson, V. N. Kotov, M. W. Meisel, D. W. Hall, G. E. Granroth, W. T. Montfrooij, S. E. Nagler, D. A. Jensen, R. Backov, M. A. Petruska, G. E. Fanucci, and D. R. Talham, Magnetic spin ladder $(\text{C}_5\text{H}_{12}\text{N})_2\text{CuBr}_4$: High-field magnetization and scaling near quantum criticality, *Phys. Rev. Lett.* **86**, 5168 (2001).
- [7] M. Klanjšek, H. Mayaffre, C. Berthier, M. Horvatić, B. Chiari, O. Piovesana, P. Bouillot, C. Kollath, E. Orignac, R. Citro, and T. Giamarchi, Controlling Luttinger liquid physics in spin ladders under a magnetic field, *Phys. Rev. Lett.* **101**, 137207 (2008).
- [8] A. Shapiro, C. P. Landee, M. M. Turnbull, J. Jornet, M. Deumal, J. J. Novoa, M. A. Robb, and W. Lewis, Synthesis, structure, and magnetic properties of an antiferromagnetic spin-ladder complex: bis(2,3-dimethylpyridinium) tetrabromocuprate, *J. Am. Chem. Soc.* **129**, 952 (2007).
- [9] M. Jeong, H. Mayaffre, C. Berthier, D. Schmidiger, A. Zheludev, and M. Horvatić, Attractive Tomonaga-Luttinger liquid in a quantum spin ladder, *Phys. Rev. Lett.* **111**, 106404 (2013).
- [10] M. Jeong, D. Schmidiger, H. Mayaffre, M. Klanjšek, C. Berthier, W. Knafo, G. Ballon, B. Vignolle, S. Krämer, A. Zheludev, and M. Horvatić, Dichotomy between attractive and repulsive Tomonaga-Luttinger liquids in spin ladders, *Phys. Rev. Lett.* **117**, 106402 (2016).
- [11] A. Paduan-Filho, R. D. Chirico, K. O. Joung, and R. L. Carlin, Field-induced magnetic ordering in uniaxial nickel systems: A second example, *J. Chem. Phys.* **74**, 4103 (1981).
- [12] S. Mukhopadhyay, M. Klanjšek, M. S. Grbić, R. Blinder, H. Mayaffre, C. Berthier, M. Horvatić, M. A. Continentino, A. Paduan-Filho, B. Chiari, and O. Piovesana, Quantum-critical spin dynamics in quasi-one-dimensional antiferromagnets, *Phys. Rev. Lett.* **109**, 177206 (2012).
- [13] S. A. Zvyagin, J. Wosnitza, C. D. Batista, M. Tsukamoto, N. Kawashima, J. Krzystek, V. S. Zapf, M. Jaime, N. F. Oliveira, and A. Paduan-Filho, Magnetic excitations in the spin-1 anisotropic Heisenberg antiferromagnetic chain system $\text{NiCl}_2\text{-4SC}(\text{NH}_2)_2$, *Phys. Rev. Lett.* **98**, 047205 (2007).
- [14] V. S. Zapf, D. Zocco, B. R. Hansen, M. Jaime, N. Harrison, C. D. Batista, M. Kenzelmann, C. Niedermayer, A. Lacerda, and A. Paduan-Filho, Bose-Einstein condensation of $S = 1$ nickel spin degrees of freedom in $\text{NiCl}_2\text{-4SC}(\text{NH}_2)_2$, *Phys. Rev. Lett.* **96**, 077204 (2006).
- [15] R. Blinder, M. Dupont, S. Mukhopadhyay, M. S. Grbić, N. Laflorencie, S. Capponi, H. Mayaffre, C. Berthier, A. Paduan-Filho, and M. Horvatić, Nuclear magnetic resonance study of the magnetic-field-induced ordered phase in

- the $\text{NiCl}_2\text{-}4\text{SC}(\text{NH}_2)_2$ compound, *Phys. Rev. B* **95**, 020404 (2017).
- [16] M. Jeong, H. Mayaffre, C. Berthier, D. Schmidiger, A. Zheludev, and M. Horvatić, Magnetic-order crossover in coupled spin ladders, *Phys. Rev. Lett.* **118**, 167206 (2017).
- [17] F. D. M. Haldane, Continuum dynamics of the 1-D Heisenberg antiferromagnet: Identification with the $O(3)$ nonlinear sigma model, *Phys. Lett. A* **93**, 464 (1983).
- [18] F. D. M. Haldane, Nonlinear field theory of large-spin Heisenberg antiferromagnets: Semiclassically quantized solitons of the one-dimensional easy-axis Néel state, *Phys. Rev. Lett.* **50**, 1153 (1983).
- [19] T. Sakai and M. Takahashi, Effect of the Haldane gap on quasi-one-dimensional systems, *Phys. Rev. B* **42**, 4537 (1990).
- [20] K. Wierschem and P. Sengupta, Quenching the Haldane gap in spin-1 Heisenberg antiferromagnets, *Phys. Rev. Lett.* **112**, 247203 (2014).
- [21] C. Broholm, G. Aeppli, Y. Chen, D. C. Dender, M. Enderle, P. R. Hammar, Z. Honda, K. Katsumata, C. P. Landee, M. Oshikawa, L. P. Regnault, D. H. Reich, S. M. Shapiro, M. Sieling, M. B. Stone, M. M. Turnbull, I. Zaliznyak, and A. Zheludev, Magnetized states of quantum spin chains, in *High Magnetic Fields: Applications in Condensed Matter Physics and Spectroscopy*, edited by C. Berthier, L. P. Lévy, and G. Martinez (Springer, Berlin, 2001), Chap. 8, pp. 211–234.
- [22] C. Rüegg, N. Cavadini, A. Furrer, H. U. Güdel, K. Krämer, H. Mutka, A. Wildes, K. Habicht, and P. Vorderwisch, Bose-Einstein condensation of the triplet states in the magnetic insulator TiCuCl_3 , *Nature (London)* **423**, 62 (2003).
- [23] R. C. Williams, W. J. A. Blackmore, S. P. M. Curley, M. R. Lees, S. M. Birnbaum, J. Singleton, B. M. Huddart, T. J. Hicken, T. Lancaster, S. J. Blundell, F. Xiao, A. Ozarowski, F. L. Pratt, D. J. Voneshen, Z. Guguchia, C. Baines, J. A. Schlueter, D. Y. Villa, J. L. Manson, and P. A. Goddard, Near-ideal molecule-based Haldane spin chain, *Phys. Rev. Res.* **2**, 013082 (2020).
- [24] P. Tin, M. J. Jenkins, J. Xing, N. Caci, Z. Gai, R. Jin, S. Wessel, J. Krzystek, C. Li, L. L. Daemen, Y. Cheng, and Z.-L. Xue, Haldane topological spin-1 chains in a planar metal-organic framework, *Nat. Commun.* **14**, 5454 (2023).
- [25] K. Mukai, H. Nagai, and K. Ishizu, The proof of a triplet ground state in the $\text{N,N}'\text{-Di-}t\text{-butyl-}m\text{-phenylenebinitroxide}$ biradical, *Bull. Chem. Soc. Jpn.* **48**, 2381 (1975).
- [26] F. Kanno, K. Inoue, N. Koga, and H. Iwamura, Persistent 1,3,5-benzenetriyltris(*N*-tert-butyl nitroxide) and its analogs with quartet ground states. Intramolecular triangular exchange coupling among three nitroxide radical centers, *J. Phys. Chem.* **97**, 13267 (1993).
- [27] F. Kanno, K. Inoue, N. Koga, and H. Iwamura, 4,6-Dimethoxy-1,3-phenylenebis(*N*-tert-butyl nitroxide) with a singlet ground state. Formal violation of a rule that *m*-phenylene serves as a robust ferromagnetic coupling unit, *J. Am. Chem. Soc.* **115**, 847 (1993).
- [28] H. Kumagai and K. Inoue, A chiral molecular based metamagnet prepared from manganese ions and a chiral triplet organic radical as a bridging ligand, *Angewan. Chem. Intl. Edit.* **38**, 1601 (1999).
- [29] H. Fischer, *Nitroxide Radicals and Nitroxide Based High-Spin Systems* (Springer, Berlin, Heidelberg, 2005).
- [30] A. Rajca, Organic diradicals and polyradicals: From spin coupling to magnetism? *Chem. Rev.* **94**, 871 (1994).
- [31] Y. Hosokoshi, K. Katoh, Y. Nakazawa, H. Nakano, and K. Inoue, Approach to a single-component ferrimagnetism by organic radical crystals, *J. Am. Chem. Soc.* **123**, 7921 (2001).
- [32] K. Katoh, Y. Hosokoshi, K. Inoue, M. Bartashevich, H. Nakano, and T. Goto, Magnetic properties of organic two-leg spin-ladder systems with $S = 1/2$ and $S = 1$, *J. Phys. Chem. Solids* **63**, 1277 (2002).
- [33] Y. Hosokoshi, Y. Nakazawa, K. Inoue, K. Takizawa, H. Nakano, M. Takahashi, and T. Goto, Magnetic properties of low-dimensional quantum spin systems made of stable organic biradicals PNNNO, F_2PNNNO , and PIMNO, *Phys. Rev. B* **60**, 12924 (1999).
- [34] P. A. Goddard, J. L. Manson, J. Singleton, I. Franke, T. Lancaster, A. J. Steele, S. J. Blundell, C. Baines, F. L. Pratt, R. D. McDonald, O. E. Ayala-Valenzuela, J. F. Corbey, H. I. Southerland, P. Sengupta, and J. A. Schlueter, Dimensionality selection in a molecule-based magnet, *Phys. Rev. Lett.* **108**, 077208 (2012).
- [35] G. M. Sheldrick, A short history of SHELX, *Acta Crystallogr. A: Found. Crystallogr.* **64**, 112 (2008).
- [36] P. Giannozzi, O. Andreussi, T. Brumme, O. Bunau, M. B. Nardelli, M. Calandra, R. Car, C. Cavazzoni, D. Ceresoli, M. Cococcioni, N. Colonna, I. Carnimeo, A. D. Corso, S. de Gironcoli, P. Delugas, R. A. DiStasio, A. Ferretti, A. Floris, G. Fratesi, G. Fugallo *et al.*, Advanced capabilities for materials modelling with Quantum ESPRESSO, *J. Phys.: Condens. Matter* **29**, 465901 (2017).
- [37] K. Berland and P. Hyldgaard, Exchange functional that tests the robustness of the plasmon description of the van der Waals density functional, *Phys. Rev. B* **89**, 035412 (2014).
- [38] K. F. Garrity, J. W. Bennett, K. M. Rabe, and D. Vanderbilt, Pseudopotentials for high-throughput DFT calculations, *Comput. Mater. Sci.* **81**, 446 (2014).
- [39] T. Cvitanic, M. Lukas, and M. S. Grbić, Two-axis goniometer for single-crystal nuclear magnetic resonance measurements, *Rev. Sci. Instrum.* **90**, 043903 (2019).
- [40] K. Momma and F. Izumi, *VESTA3* for three-dimensional visualization of crystal, volumetric and morphology data, *J. Appl. Crystallogr.* **44**, 1272 (2011).
- [41] M. Faridfar and J. Vahedi, Thermodynamic behavior of spin-1 Heisenberg chain: A comparative study, *J. Supercond. Novel Magn.* **35**, 519 (2022).
- [42] J. M. Law, H. Benner, and R. K. Kremer, Padé approximations for the magnetic susceptibilities of Heisenberg antiferromagnetic spin chains for various spin values, *J. Phys.: Condens. Matter* **25**, 065601 (2013).
- [43] Padé-approximation coefficients: $A_1 = 0.679$, $A_2 = 1.270$, $A_3 = 0.655$, $A_4 = 0.141$, $A_5 = 0.088$, $B_1 = 1.600$, $B_2 = 2.653$, $B_3 = 2.516$, $B_4 = 1.678$, $B_5 = 0.420$, $B_6 = 0.041$.
- [44] O. Kahn, *Molecular Magnetism* (Wiley-VCH, New York, 1993).
- [45] K. Wierschem and P. Sengupta, Characterizing the Haldane phase in quasi-one-dimensional spin-1 Heisenberg antiferromagnets, *Mod. Phys. Lett. B* **28**, 1430017 (2014).

- [46] R. Chitra and T. Giamarchi, Critical properties of gapped spin-chains and ladders in a magnetic field, *Phys. Rev. B* **55**, 5816 (1997).
- [47] K. Nagata and Y. Tazuke, Short range order effects on EPR frequencies in Heisenberg linear chain antiferromagnets, *J. Phys. Soc. Jpn.* **32**, 337 (1972).
- [48] K. Nagata, Short range order effects on EPR frequencies in antiferromagnets, *Physica B+C* **86-88**, 1283 (1977).
- [49] M. Oshikawa and I. Affleck, Low-temperature electron spin resonance theory for half-integer spin antiferromagnetic chains, *Phys. Rev. Lett.* **82**, 5136 (1999).
- [50] M. Oshikawa and I. Affleck, Electron spin resonance in $S = \frac{1}{2}$ antiferromagnetic chains, *Phys. Rev. B* **65**, 134410 (2002).
- [51] H. Ohta, Experimental studies of Dzyaloshinskii–Moriya interaction in quantum spin systems: High-frequency high-field electron spin resonance (ESR) measurements, *J. Phys. Soc. Jpn.* **92**, 081003 (2023).
- [52] M. Herak, A. Zorko, D. Arčon, A. Potočnik, M. Klanjšek, J. van Tol, A. Ozarowski, and H. Berger, Symmetric and antisymmetric exchange anisotropies in quasi-one-dimensional CuSe_2O_5 as revealed by ESR, *Phys. Rev. B* **84**, 184436 (2011).
- [53] S. C. Furuya and M. Sato, Electron spin resonance in quasi-one-dimensional quantum antiferromagnets: Relevance of weak interchain interactions, *J. Phys. Soc. Jpn.* **84**, 033704 (2015).
- [54] J. R. Durig, S. M. Craven, J. H. Mulligan, C. W. Hawley, and J. Bragin, Low frequency modes in molecular crystals. XIX. Methyl torsions and barriers to internal rotation of some three top molecules with C_3 symmetry, *J. Chem. Phys.* **58**, 1281 (1973).
- [55] A. Bencini and D. Gatteschi, *Electron Paramagnetic Resonance of Exchange Coupled Systems* (Springer, Berlin, Heidelberg, 1990).
- [56] J. E. Gulley, D. Hone, D. J. Scalapino, and B. G. Silbernagel, Exchange narrowing: Magnetic resonance line shapes and spin correlations in paramagnetic KMnF_3 , RbMnF_3 , and MnF_2 , *Phys. Rev. B* **1**, 1020 (1970).
- [57] J. H. Van Vleck, The dipolar broadening of magnetic resonance lines in crystals, *Phys. Rev.* **74**, 1168 (1948).
- [58] K. T. McGregor and Z. G. Soos, Anisotropic exchange in linear chain complexes of copper(II), *J. Chem. Phys.* **64**, 2506 (1976).
- [59] E. Orignac, R. Citro, and T. Giamarchi, Critical properties and Bose-Einstein condensation in dimer spin systems, *Phys. Rev. B* **75**, 140403(R) (2007).
- [60] M. Dupont, S. Capponi, and N. Laflorencie, Temperature dependence of the NMR relaxation rate $1/T_1$ for quantum spin chains, *Phys. Rev. B* **94**, 144409 (2016).
- [61] M. Dupont, S. Capponi, N. Laflorencie, and E. Orignac, Dynamical response and dimensional crossover for spatially anisotropic antiferromagnets, *Phys. Rev. B* **98**, 094403 (2018).
- [62] M. Horvatić, M. Klanjšek, and E. Orignac, Direct determination of the Tomonaga-Luttinger parameter K in quasi-one-dimensional spin systems, *Phys. Rev. B* **101**, 220406(R) (2020).
- [63] K. Nawa, M. Takigawa, M. Yoshida, and K. Yoshimura, Anisotropic spin fluctuations in the quasi one-dimensional frustrated magnet LiCuVO_4 , *J. Phys. Soc. Jpn.* **82**, 094709 (2013).
- [64] A. Aharoni, Demagnetizing factors for rectangular ferromagnetic prisms, *J. Appl. Phys.* **83**, 3432 (1998).
- [65] S. A. Southern, D.-J. Liu, P. Chatterjee, Y. Li, and F. A. Perras, ^1H chemical shift anisotropy: A high sensitivity solid-state NMR dynamics probe for surface studies? *Phys. Chem. Chem. Phys.* **25**, 5348 (2023).
- [66] A. M. Orendt, J. Z. Hu, Y.-J. Jiang, J. C. Facelli, W. Wang, R. J. Pugmire, C. Ye, and D. M. Grant, Solid-state ^{13}C NMR measurements in methoxynaphthalenes: Determination of the substituent chemical shift effects in the principal values, *J. Phys. Chem. A* **101**, 9169 (1997).
- [67] F. Colhoun, R. Armstrong, and G. Rutledge, Chemical shift tensors for the aromatic carbons in polystyrene, *Polymer* **43**, 609 (2002).
- [68] R. M. Konik and P. Fendley, Haldane-gapped spin chains as Luttinger liquids: Correlation functions at finite field, *Phys. Rev. B* **66**, 144416 (2002).
- [69] B. Bleaney and K. D. Bowers, Anomalous paramagnetism of copper acetate, *Proc. R. Soc. London A* **214**, 451 (1952).